Composite Structures 371 (2025) 119508

Contents lists available at ScienceDirect

Composite Structures

journal homepage: www.elsevier.com/locate/compstruct

Variable-order framework for aeroelastic flutter analysis of laminated composite wings

Dario Campagna, Ivano Benedetti *, Vincenzo Gulizzi *

Department of Engineering, University of Palermo, Viale delle Scienze, Edificio 8, 90128, Palermo, Italy

ARTICLE INFO

Keywords:
Variable kinematics
Discontinuous Galerkin method
Unsteady vortex lattice method
Flutter analysis
Computational aeroelasticity
Composite materials

ABSTRACT

This work presents a novel computational framework for aeroelastic flutter analysis of laminated composite wings. The proposed methodology combines a discontinuous Galerkin (DG) method for structural analysis with the unsteady vortex lattice method (UVLM) for aerodynamic modeling. A specific and novel feature of the framework is a variable-order kinematic model, which enables the seamless analysis of lifting structures through different structural theories, such as beam and plate models. The coupling between the structural and aerodynamic models is performed under the assumptions of small structural deformations and aerodynamic perturbations. The framework has been implemented and validated against various experimental or numerical benchmark results for single- and multi-layer configurations available in the literature or obtained by employing industry-standard finite element codes for aeroelastic analysis. The obtained results show the accuracy and robustness of the proposed methodology, highlighting the capability of variable-order DG approximations to achieve faster convergence rates with respect to standard finite element methods, in terms of degrees of freedom. This makes the framework a powerful tool for rapid aeroelastic analysis of composite structures in the early stages of aircraft design.

1. Introduction

The ability to predict the response of solids or structures under the action of fluid flows is relevant for the design and analysis of advanced structures, including large civil infrastructures [1,2], turbomachinery [3], biomedical devices [4], wind turbines [5,6], and aircraft components [7]. Among different fluid–structure interaction (FSI) phenomena, in aeronautics and aerospace applications, *flutter* is a self-sustained oscillation caused by the interplay of elastic, inertial and aerodynamic forces, which may lead to catastrophic consequences, if the structure is not suitably designed [8–10].

Multilayered composite materials allow engineers to design structures with greater safety margins with respect to aeroelastic instabilities, enabling the so-called aeroelastic tailoring [11–13] whereby, through the selection of appropriate lamination sequences, it is indeed possible, to some extent, to modify the structure aeroelastic properties, such as divergence or flutter speed. However, aeroelastic problems involving multilayered composite plates with general stacking sequences can rarely be solved analytically and often require numerical solution strategies.

Different approaches for aeroelastic modeling have been proposed and developed in the literature, at different levels of fidelity from both the aerodynamic and the structural points of view. The choice of a particular modeling approach varies based on the objectives of the analysis and the design phase. High-fidelity models based on the coupling between Computational Fluid Dynamics (CFD) and Computational Structural Dynamics (CSD) have been used to investigate several FSI problems in different engineering fields, e.g. bridges [14], helicopter and wind turbine blades [15], the stability of turbo-machinery components [16–18], the bio-mechanics of heart valves [19], as well as for aircraft analysis and design [20–22]. High-fidelity methods provide highly accurate solutions but come with significant demands on processing time and computational resources [23]. However, during the design phase, such a high level of accuracy is often unnecessary, and low- or medium-fidelity methods can offer better efficiency while still meeting the requirements of the analysis.

Indeed, different strategies have been adopted, with the aim of reducing the overall computational cost. From a structural standpoint, equivalent plate models [24,25] have been coupled with CFD for the analysis of complex aircraft structures; 1D finite element models (FEM) have been coupled with CFD for the aeroelastic analysis of turbine blades [26–28] and high aspect-ratio wings [29–31]. On the other hand, to reduce the cost of the aerodynamic computations, alternative approaches with respect to CFD have been adopted, such as the well-known vortex lattice method (VLM) or the doublet lattice method

* Corresponding authors.
E-mail addresses: ivano.benedetti@unipa.it (I. Benedetti), vincenzo.gulizzi@unipa.it (V. Gulizzi).

https://doi.org/10.1016/j.compstruct.2025.119508
Received 28 April 2025; Received in revised form 4 July 2025; Accepted 22 July 2025

(DLM), which, may provide fast and reasonably accurate numerical assessments in design operational conditions despite being limited to specific flow regimes [32], i.e. low-speed, high-Reynolds flows.

Although methods like VLM and the DLM have long been employed in aerodynamic and aeroelastic analyses, their use has become increasingly widespread in recent years due to their ability to integrate efficiently with structural models [33–40]. This effective coupling allows for reliable and computationally efficient simulations, making these methods particularly attractive for preliminary design phases and iterative optimization processes where balancing accuracy and resource consumption is essential.

In this work, a novel framework for computational aeroelasticity, used for flutter analysis of laminated composite wing is developed and validated. The novelty of the method is the coupling between a recently-developed Interior Penalty discontinuous Galerkin method (DG) for structural analysis and the unsteady vortex lattice method (UVLM) for unsteady aerodynamic modeling. The proposed structural formulation is based on a variable-order kinematic model, which allows adopting different structural theories, including beam [38,41], plate [42,43] and shell [44] theories, and enabling the selection of different expansion orders in the displacement approximation, thus reducing the number of degree of freedom required to attain a desired level of accuracy and providing a tool for fast, low-cost flutter analysis.

The paper is organized as follows. Section 2 describes the aeroelastic problem analyzed in this study: first, the basic equations of kinematics and constitutive relations, the adopted variable-order structural theory approximation, and the structural governing equations; then, the coupling between the structural and aerodynamic models, which, under some specific assumptions, leads to a monolithic solution for solving flutter problems. Section 3 validate the proposed numerical framework and show several results of laminated wing configurations compared with both numerical and experimental data from the literature to assess its accuracy. Section 4 critically discusses the main features of the proposed methodology, identifying directions for further investigation and development. Eventually, *Conclusions* are drawn.

2. Methods

In this section the key items of the formulation are presented and discussed.

2.1. Problem definition

A general rectangular laminated wing, schematically represented in (Fig. 1a), is considered. The wing is described using a global cartesian reference system $Ox_1x_2x_3$ centered at the quarter chord of the root section where the axis x_1 is aligned with the direction of flight and parallel to the root chord, the axis x_2 is perpendicular to the root chord and the axis x_3 is consequently defined as normal to the plane x_1x_2 pointing towards the low pressure side of the wing. The undeformed rectangular wing lays on the plane x_1x_2, see (Fig. 1b), and has reference surface S, wingspan b, chord c, and thickness ζ. The structure is immersed in a free-stream having an aerodynamic speed V_∞ oriented in the opposite direction of x_1 with an angle α with respect to the root chord. The generic rectangular laminated plate is assembled using N_ℓ unidirectional composite laminae of thickness $\zeta^{\langle\ell\rangle}$ in which a local material coordinate system $O\tilde{x}_1^{\langle\ell\rangle}\tilde{x}_2^{\langle\ell\rangle}\tilde{x}_3^{\langle\ell\rangle}$ is defined such that $\tilde{x}_1^{\langle\ell\rangle}$ forms an angle $\theta^{\langle\ell\rangle}$ with the global axis x_1 and $\tilde{x}_3^{\langle\ell\rangle}$ coincides with the axis x_3, as shown in (Fig. 1c).

The wake shadded by the wing is represented following the *Unsteady Vortex Lattice Method*, that enable solving unsteady potential-flow problems [32] considering both wing motion and wake roll-up effects [34,45] . The wake geometry is generated by vortex scattered from the trailing edge of the wing and spreaded in the flight direction with a velocity field composed by the free-stream velocity and the local velocity induced by the surrounding vortexes. In the present computational framework a frozen wake geometry approach is used: the wake generated by the wing is computed apriori and used to compute the strength of the vortexes in the subsequent flutter eigenvalue problem. More detail on the unsteady aerodynamic field and the vortex strengths computation are given in subsection *Aerodynamic model*.

2.2. Structural model

In this section, the features of the structural model with variable-order kinematics are presented.

2.2.1. Basic equations

The considered wing, subjected to body forces $\overline{\boldsymbol{b}} = (\overline{b}_1, \overline{b}_2, \overline{b}_3)^\intercal$ acting over its volume D, is assumed to undergo small linear-elastic displacements, denoted by $\boldsymbol{u} = (u_1, u_2, u_3)^\intercal$, with the associated small strains $\boldsymbol{\gamma} = (\gamma_{11}, \gamma_{22}, \gamma_{33}, \gamma_{23}, \gamma_{31}, \gamma_{12})^\intercal$ and stresses $\boldsymbol{\sigma} = (\sigma_{11}, \sigma_{22}, \sigma_{33}, \sigma_{23}, \sigma_{31}, \sigma_{12})^\intercal$, expressed in Voigt notation. The wing is constrained by essential boundary conditions $\boldsymbol{u} = \boldsymbol{0}$ for $\boldsymbol{x} \in \partial D_u$, where ∂D_u denotes the root section of the wing, i.e. $\partial D_u \equiv \{\boldsymbol{x} \in D \ : \ x_2 = 0\}$, while the other regions of the wing boundary are traction-free; as it will be shown in Section 2.3, the aerodynamic forces are transferred to the structure as body forces.

Under the small-strain assumption, the strain displacement relationship can be written as

$$\boldsymbol{\gamma} = \boldsymbol{\mathcal{I}}_1 \frac{\partial \boldsymbol{u}}{\partial x_1} + \boldsymbol{\mathcal{I}}_2 \frac{\partial \boldsymbol{u}}{\partial x_2} + \boldsymbol{\mathcal{I}}_3 \frac{\partial \boldsymbol{u}}{\partial x_3}, \tag{1}$$

where the definition of the matrices $\boldsymbol{\mathcal{I}}_1$, $\boldsymbol{\mathcal{I}}_2$ and $\boldsymbol{\mathcal{I}}_3$, containing ones and zeros only, can be found in Ref. [46]. Considering the constitutive material behavior, it is assumed that the ℓ-th lamina in the local material reference system behave as an orthotropic material, whose stress–strain relationship may be written as

$$\tilde{\boldsymbol{\sigma}}^{\langle\ell\rangle} = \tilde{\boldsymbol{c}}^{\langle\ell\rangle} \tilde{\boldsymbol{\gamma}}^{\langle\ell\rangle}, \tag{2}$$

where $\tilde{\boldsymbol{c}}^{\langle\ell\rangle}$ is a 6×6 matrix that contains the stiffness coefficients and is computed as

$$\tilde{\boldsymbol{c}}^{\langle\ell\rangle} = (\tilde{\boldsymbol{s}}^{\langle\ell\rangle})^{-1} \quad \text{with}$$

$$\tilde{\boldsymbol{s}}^{\langle\ell\rangle} \equiv \begin{bmatrix} 1/E_1 & -\nu_{12}/E_1 & -\nu_{13}/E_1 & 0 & 0 & 0 \\ -\nu_{12}/E_1 & 1/E_2 & -\nu_{23}/E_2 & 0 & 0 & 0 \\ -\nu_{13}/E_1 & -\nu_{23}/E_2 & 1/E_3 & 0 & 0 & 0 \\ 0 & 0 & 0 & 1/G_{23} & 0 & 0 \\ 0 & 0 & 0 & 0 & 1/G_{13} & 0 \\ 0 & 0 & 0 & 0 & 0 & 1/G_{12} \end{bmatrix}^{\langle\ell\rangle} \tag{3}$$

being E_k the Young moduli, ν_{kl} the Poisson ratios, and G_{kl} the shear moduli. It is worth noting that the constitutive equation appearing in Eq. (2) can be written in the wing global reference system as

$$\boldsymbol{\sigma}^{\langle\ell\rangle} = \boldsymbol{c}^{\langle\ell\rangle} \boldsymbol{\gamma}^{\langle\ell\rangle}, \tag{4}$$

where $\boldsymbol{\sigma}^{\langle\ell\rangle} = \boldsymbol{T}_\sigma^{-1}\left(\theta^{\langle\ell\rangle}\right)\tilde{\boldsymbol{\sigma}}^{\langle\ell\rangle}$, $\boldsymbol{\gamma}^{\langle\ell\rangle} = \boldsymbol{T}_\gamma^{-1}\left(\theta^{\langle\ell\rangle}\right)\tilde{\boldsymbol{\gamma}}^{\langle\ell\rangle}$ and $\boldsymbol{c}^{\langle\ell\rangle} = \boldsymbol{T}_\sigma^{-1}\left(\theta^{\langle\ell\rangle}\right)\tilde{\boldsymbol{c}}^{\langle\ell\rangle}\boldsymbol{T}_\gamma\left(\theta^{\langle\ell\rangle}\right)$, being $\boldsymbol{T}_\sigma$ and $\boldsymbol{T}_\gamma$ suitable transformation matrices whose expression can be found in Ref. [47].

2.2.2. Variational formulation

The weak form of structural dynamic governing equations can be obtained from the d'Alembert principle, by expressing the inertial loads as distributed volume forces in the classical form of the principle of virtual displacements as follows

$$\int_D \delta\boldsymbol{u}^\intercal \rho \frac{\partial^2 \boldsymbol{u}}{\partial t^2}\,\mathrm{d}D + \int_D \delta\boldsymbol{\gamma}^\intercal \boldsymbol{\sigma}\,\mathrm{d}D = \int_D \delta\boldsymbol{u}^\intercal \overline{\boldsymbol{b}}\,\mathrm{d}D, \tag{5}$$

where ρ is the local structural material density, $\partial^2\boldsymbol{u}/\partial t^2$ denotes the second derivative of the displacement field with respect to time, and $\delta(\bullet)$ denotes the first variation of the quantity $\bullet$. It is worth noting that,

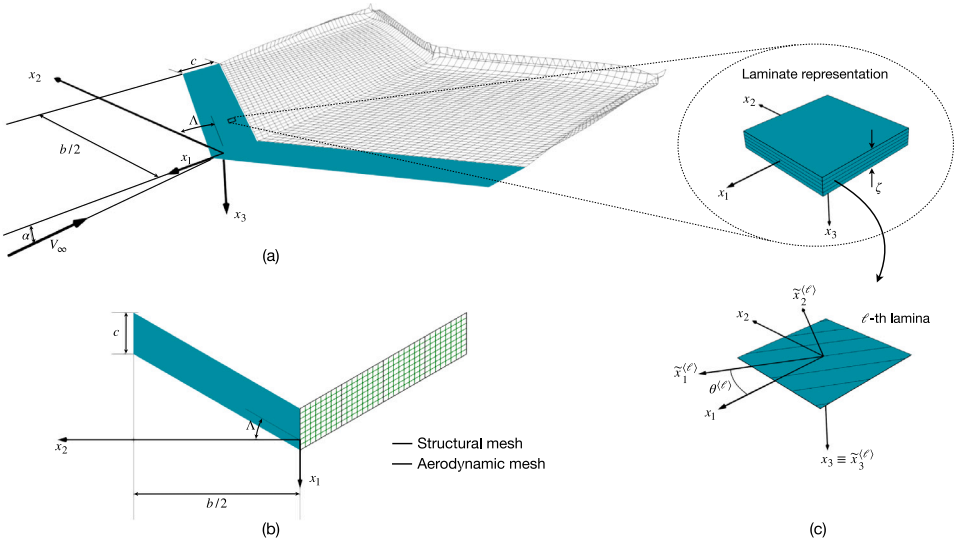

Fig. 1. Wing structure: (a) geometry definition and wake representation, (b) wing planform with structural and aerodynamic mesh representation; (c) laminate representation and definition of local material coordinate reference system.

based on the assumption introduced in Sec. 2.2.1, no surface tractions are included in Eq. (5). Upon substitution of Eqs. (1) and (4) into Eq. (5), the principle of virtual displacement expressed in terms of the displacement field $\boldsymbol{u}$ reads as

$$\int_D \delta\boldsymbol{u}^\intercal \rho \frac{\partial^2 \boldsymbol{u}}{\partial t^2}\,\mathrm{d}D + \int_D \frac{\partial \delta\boldsymbol{u}^\intercal}{\partial x_k}\boldsymbol{c}_{kl}\frac{\partial \boldsymbol{u}}{\partial x_l}\,\mathrm{d}D = \int_D \delta\boldsymbol{u}^\intercal \bar{\boldsymbol{b}}\,\mathrm{d}D, \tag{6}$$

where $\boldsymbol{c}_{kl} \equiv \boldsymbol{I}_k^\intercal \boldsymbol{c}\, \boldsymbol{I}_l$ are 3×3 matrices containing suitable subsets of the stiffness coefficients. It is worth noting that the integrals appearing in Eq. (6) are evaluate considering the different properties of the laminae in the stacking sequence, i.e., for a plate made of N_ℓ laminae, $\int_D \bullet\,\mathrm{d}D \equiv \sum_{\ell=1}^{N_\ell} \int_{D^{\langle\ell\rangle}} \bullet^{\langle\ell\rangle}\mathrm{d}D$. Additionally, Einstein summation over repeated subscripts $k, l \in \{1,2,3\}$ is employed.

2.2.3. Geometry description and variable-order kinematics

To account for different wing geometries, including swept wings, a set of parametric coordinates ξ_1, ξ_2 and ξ_3 is introduced such that a generic point $\boldsymbol{x} \in D$ may be described as

$$\boldsymbol{x}\left(\xi_1,\xi_2,\xi_3\right) = \boldsymbol{x}_R + \left(\boldsymbol{x}_T - \boldsymbol{x}_R\right)\xi_2 + \left(c/4 - \xi_1\right)\widehat{\boldsymbol{i}} - \xi_3\widehat{\boldsymbol{k}}, \tag{7}$$

where $\xi_1 \in [0, c]$, $\xi_2 \in [0,1]$, $\xi_3 \in \left[-\zeta/2, \zeta/2\right]$, $\widehat{\boldsymbol{i}} \equiv (1,0,0)^\intercal$ and $\widehat{\boldsymbol{k}} \equiv (0,0,1)^\intercal$, and $\boldsymbol{x}_R$ and $\boldsymbol{x}_T$ are the quarter-chord points at the wing root and the wing tip, respectively.

The kinematic assumptions are implemented by first subdividing the wing volume D into a collection of N_e elements, i.e., $D = \bigcup_{e=1}^{N_e} D^e$, where D^e is the generic eth element, and then expressing the kth displacement component u_k^h over D^e in terms of the parametric coordinates ξ_1, ξ_2, and ξ_3 as

$$u_k^h(t, \boldsymbol{x} \in D^e) = \sum_{i_1=0}^{p_1}\sum_{i_2=0}^{p_2}\sum_{i_3=0}^{p_3} b_{i_1}^e(\xi_1) b_{i_2}^e(\xi_2) b_{i_3}^e(\xi_3) X_{i_1 i_2 i_3}^{e,k}(t), \tag{8}$$

where the superscript h indicates that u_k^h is an approximation of u_k, $b_{i_1}^e(\xi_1)$, $b_{i_2}^e(\xi_2)$, and $b_{i_3}^e(\xi_3)$ are the one-dimensional basis functions chosen to express the chord-wise, span-wise, and thickness-wise approximations, respectively, p_1, p_2, and p_3 are the corresponding approximation orders, and $X_{i_1 i_2 i_3}^{e,k}$ are the associated time-dependent unknown coefficients. Eq. (8) can be written in compact form as

$$\boldsymbol{u}^h(t, \boldsymbol{x} \in D^e) = \boldsymbol{B}^e(\xi_1,\xi_2,\xi_3)\boldsymbol{X}^e(t), \tag{9}$$

where $\boldsymbol{X}^e$ is a $N_u N_p$-dimensional vector collecting the unknowns coefficients, and $\boldsymbol{B}^e$ is a $N_u \times N_u N_p$ matrix collecting the basis functions with $N_u = 3$ and $N_p = (1+p_1)(1+p_2)(1+p_3)$. It is worth noting that the ith element of vector $\boldsymbol{X}^e$, namely $X_i^{e,k}$, is the unknown coefficient associated to ith basis function $B_i^e(\xi_1,\xi_2,\xi_3)$ for the kth displacement component, with the index i being associated with the tuple (i_1, i_2, i_3). In this work, the same expansion order $p = p_1 = p_2 = p_3$ is associated with the three displacement components, although more general choices could be made, as for example done in the case of the first-order shear deformation theory [47]. The selection of different kinematic assumptions allows adopting structural models of different orders and makes the proposed numerical method highly flexible, as in the Carrera Unified Formulation (CUF) [48] or in the Generalize Unified Formulation [49]. Moreover, it is worth noting the different kinematic approximations can be seamlessly adopted over contiguous elements, as inter-element continuity conditions are enforced in a weak integral sense.

2.2.4. Discontinuous Galerkin formulation

The kinematic approximation in Eq. (8) is not limited to a specific set of basis functions and, in general, it can vary from element to element. To enforce inter-element continuity and boundary conditions, a recently-developed Interior Penalty discontinuous Galerkin formulation for the elastodynamic behavior of plates and shells [44,46] is employed and briefly recalled in this section. Starting from Eq. (6), it is possible to show that the associated DG formulation may be stated as

$$Find \quad \boldsymbol{u}^h \in (\mathcal{V}^h)^{N_u} \quad such\ that \quad B_{\mathsf{M}}(\boldsymbol{v}, \boldsymbol{u}^h) + B_{\mathsf{K}}(\boldsymbol{v}, \boldsymbol{u}^h) = L(\boldsymbol{v}, \boldsymbol{b}) \qquad \forall \boldsymbol{v} \in (\mathcal{V}^h)^{N_u} \tag{10}$$

where $(\mathcal{V}^h)^{N_u}$ is the space of N_u-dimensional discontinuous vector fields defined on the mesh elements and $\boldsymbol{v} \equiv (v_1, v_2, v_3)^\intercal$ are the test functions; additionally, in Eq. (10), the following bilinear and linear terms have been introduced

$$B_{\mathsf{M}}(\boldsymbol{v}, \boldsymbol{u}^h) \equiv \int_{\mathcal{D}^h} \boldsymbol{v}^\intercal \rho \frac{\partial^2 \boldsymbol{u}^h}{\partial t^2}\,\mathrm{d}D, \tag{11}$$

$$\begin{aligned} B_{\mathsf{K}}(\boldsymbol{v}, \boldsymbol{u}^h) \equiv & \int_{\mathcal{D}^h} \frac{\partial \boldsymbol{v}^\intercal}{\partial x_k}\boldsymbol{c}_{kl}\frac{\partial \boldsymbol{u}^h}{\partial x_l}\,\mathrm{d}D + \\ & - \int_{\mathcal{I}^h} \left[[\![\boldsymbol{v}]\!]_k^\intercal \left\{ \boldsymbol{c}_{kl}\frac{\partial \boldsymbol{u}^h}{\partial x_l}\right\} + \left\{ \frac{\partial \boldsymbol{v}^\intercal}{\partial x_k}\boldsymbol{c}_{kl}\right\} [\![\boldsymbol{u}^h]\!]_l \right] \mathrm{d}D + \int_{\mathcal{I}^h} \mu [\![\boldsymbol{v}]\!]_k^\intercal [\![\boldsymbol{u}^h]\!]_k\,\mathrm{d}\partial D + \\ & - \int_{\partial\mathcal{D}_u^h} \left[n_k \boldsymbol{v}^\intercal \left(\boldsymbol{c}_{kl}\frac{\partial \boldsymbol{u}^h}{\partial x_l}\right) + \left(\frac{\partial \boldsymbol{v}^\intercal}{\partial x_k}\boldsymbol{c}_{kl}\right)\boldsymbol{u}^h n_l \right] \mathrm{d}\partial D + \int_{\partial\mathcal{D}_u^h} \mu \boldsymbol{v}^\intercal \boldsymbol{u}^h\,\mathrm{d}\partial D \end{aligned} \tag{12}$$

and

$$L(\boldsymbol{v}, \boldsymbol{b}) \equiv \int_{\mathcal{D}^h} \boldsymbol{v}^\intercal \boldsymbol{b}\,\mathrm{d}D, \tag{13}$$

where μ, appearing in Eq. (12), is a penalty parameter that, if selected as proportional to c/h, with c denoting a representative material stiffness constant and h a representative mesh size, ensures the optimal convergence of the DG scheme [46,50]. The integrals appearing in Eqs. (11), (12) and (13) are generally referred to as *broken integrals* and are defined as

$$\int_{\mathcal{D}^h} \bullet \, \mathrm{d}\mathcal{D} \equiv \sum_{e=1}^{N_e} \int_{\mathcal{D}^e} \bullet^e \, \mathrm{d}\mathcal{D}, \quad \int_{\partial\mathcal{D}_u^h} \bullet \, \mathrm{d}\partial\mathcal{D} \equiv \sum_{e=1}^{N_e} \int_{\partial\mathcal{D}_u^e} \bullet^e \, \mathrm{d}\partial\mathcal{D}, \quad \text{and}$$
$$\int_{\mathcal{I}^h} \bullet \, \mathrm{d}\partial\mathcal{D} \equiv \sum_{i=1}^{N_i} \int_{\mathcal{I}^i} \bullet^i \, \mathrm{d}\partial\mathcal{D}, \tag{14}$$

where $\partial\mathcal{D}_u^e$ is the portion of the boundary of the eth element in which Dirichlet boundary conditions are enforced, while $\mathcal{I}^i$ is a generic interface between two contiguous elements and $\mathcal{I}^h \equiv \bigcup_{i=1}^{N_i} \mathcal{I}^i$ denotes the collection of all the inter-element interfaces associated with the considered mesh. Moreover, in Eq. (12), n_k is the kth components of the unit normal vector at the element boundaries, while the terms $\{\bullet\}$ and $[\![\bullet]\!]_k$ denote the average and jump operators, respectively, defined at the interface i between two adjacent elements e and e' as

$$\{\bullet\}^i \equiv \frac{1}{2}\left(\bullet^e + \bullet^{e'}\right) \quad \text{and} \quad [\![\bullet]\!]_k^i \equiv \bullet^e n_k^e + \bullet^{e'} n_k^{e'}. \tag{15}$$

Eventually, by letting $\boldsymbol{v}$ span all the basis functions contained in $(\mathcal{V}^h)^{N_u}$, the following system of second-order ordinary differential equations is obtained

$$\mathbf{M}_\mathsf{S}\ddot{\mathbf{X}}(t) + \mathbf{K}_\mathsf{S}\mathbf{X}(t) = \mathbf{F}(t), \tag{16}$$

where the overdots denote derivatives with respect to time, $\mathbf{M}_\mathsf{S}$ is the mass matrix stemming from the term $B_\mathsf{M}(\boldsymbol{v}, \boldsymbol{u}^h)$ in Eq. (11), $\mathbf{K}_\mathsf{S}$ is the stiffness matrix stemming from the term $B_\mathsf{K}(\boldsymbol{v}, \boldsymbol{u}^h)$ in Eq. (12), $\mathbf{F}$ is the right-hand side stemming from the term $L(\boldsymbol{v}, \bar{\boldsymbol{b}})$ defined in Eq. (13) and $\mathbf{X}$ is the vector containing the unknown structural degrees of freedom associated with the considered structural theory and DG formulation.

2.3. Aerodynamic model

The aerodynamics loads generated on the wing structure are computed under the assumption of the potential-flow theory using the UVLM [32], following the approach proposed by Murua et al. [34], whereby the UVLM is first employed to generate the wake shed by the wing and then to derive the linearized aerodynamic equations for flutter analysis.

In the UVLM, the wing and the wake are modeled as a set of N_b bound ring vortexes and a set of N_w shed ring vortexes, respectively. The intensities of the bound vortexes are collected into the vector $\boldsymbol{\Gamma}$ and represent the unknowns of the aerodynamic problem. The intensities of the shed vortexes are instead known and determined as functions of the bound vortexes at the trailing edge of the wing. At the generic time t, the impenetrability condition leads to the following system of equations governing the evolution of the bound vortex intensities

$$\mathbf{A}\boldsymbol{\Gamma}(t) = \mathbf{b} + \mathbf{b}_w(t) + \mathbf{b}_\mathsf{S}(t), \tag{17}$$

where $\mathbf{A}$ is the aerodynamic coefficient matrix representing the interactions among the bound vortexes, and $\mathbf{b}$, $\mathbf{b}_w$ and $\mathbf{b}_\mathsf{S}$ are the right-hand side vectors accounting for the effect of the free-stream velocity $\boldsymbol{V}_\infty$, the shed wake and the structural motion, respectively. The reader interested in the explicit expression of each of these terms is referred to Refs. [32,34].

Once the intensities of the bound vortexes have been determined, the force $\boldsymbol{f}^j$ generated by jth vortex is evaluated as

$$\boldsymbol{f}^j = \rho_\infty \boldsymbol{v}^j \times \boldsymbol{l}^j \gamma^j + \rho_\infty S^j \boldsymbol{n}_0^j \dot{\Gamma}^j, \tag{18}$$

where ρ_∞ is the air density, S^j and $\boldsymbol{l}^j$ are the area and the vector associated with the leading segment, respectively, of the jth bound vortex, and γ^j is the net circulation intensity at the leading segment of the considered vortex, coinciding with Γ^j if the jth vortex is at the wing leading edge, or otherwise given by the difference of the circulation intensities of two chord-wise contiguous vortexes.

2.4. Flutter analysis

The flutter analysis comprises the solution and stability analysis of a small-perturbation problem around a reference configuration. From the structural point of view, since small strains/displacements are assumed, the reference configuration coincides with the undeformed wing. On the other hand, the aerodynamic reference configuration is represented by the geometry of the bound vortexes and the wake shed by the undeformed wing and computed via the UVLM.

Based on the above assumptions, the structural degrees of freedom $\mathbf{X}(t)$ appearing in Eq. (16) and the aerodynamic degrees of freedom $\boldsymbol{\Gamma}(t)$ appearing in Eq. (17) may be written as $\mathbf{X}(t) = \overline{\mathbf{X}} + \widetilde{\mathbf{X}}e^{\lambda t}$ and $\boldsymbol{\Gamma}(t) = \overline{\boldsymbol{\Gamma}} + \widetilde{\boldsymbol{\Gamma}}e^{\lambda t}$, where the overbar denotes quantities associated with the reference configuration, the tilde denotes the perturbed quantities, and $\lambda \equiv \sigma + i\omega$ the complex eigenvalue associated with the small-perturbation analysis. Therefore, upon recalling that the right-hand side of Eq. (16) depends on the aerodynamic loads given in terms of $\boldsymbol{\Gamma}$ through Eq. (18), while the structural deformation affects Eq. (17) by determining the geometry of the bound vortexes, the following coupled system of equations may be written

$$\begin{cases} (\lambda^2\mathbf{M}_\mathsf{S} + \mathbf{K}_\mathsf{S})\widetilde{\mathbf{X}} = (\mathbf{F}_\Gamma + \lambda\mathbf{F}_{\dot{\Gamma}})\widetilde{\boldsymbol{\Gamma}} \\ \widetilde{\mathbf{A}}(\lambda)\,\widetilde{\boldsymbol{\Gamma}} = (\mathbf{b}_\mathsf{X} + \lambda\mathbf{b}_{\mathsf{S}\dot{\mathsf{X}}})\widetilde{\mathbf{X}} \end{cases} \tag{19}$$

In Eq. (19), under the small-perturbation approximation, it has been assumed that the right-hand side $\mathbf{F}(t)$ of Eq. (16) may be linearized as $\mathbf{F}(t) \approx \overline{\mathbf{F}} + (\mathbf{F}_\Gamma + \lambda\mathbf{F}_{\dot{\Gamma}})\widetilde{\boldsymbol{\Gamma}}e^{\lambda t}$, the terms $\mathbf{b}(t)$ and $\mathbf{b}_\mathsf{S}(t)$ may be linearized as $\mathbf{b}(t) \approx \overline{\mathbf{b}} + \mathbf{b}_\mathsf{X}\widetilde{\mathbf{X}}e^{\lambda t}$ and $\mathbf{b}_\mathsf{S}(t) \approx \lambda\mathbf{b}_{\mathsf{S}\dot{\mathsf{X}}}\widetilde{\mathbf{X}}e^{\lambda t}$, and the term $\mathbf{b}_w(t)$ may be written as $\mathbf{b}_w(t) \approx \overline{\mathbf{b}}_w + \mathbf{W}(\lambda)\widetilde{\boldsymbol{\Gamma}}e^{\lambda t}$, with the matrix $\mathbf{W}(\lambda)$ accounting for the fact that the wake is shed by trailing edge bound vortexes and contributing to the aerodynamic coefficient matrix $\widetilde{\mathbf{A}}(\lambda)$ [34]. It is also worth noting that, to obtain Eq. (19), the terms $\overline{\mathbf{X}}$ and $\overline{\boldsymbol{\Gamma}}$ have been cancelled out and the term $e^{\lambda t}$ has been dropped.

A further rearrangement of Eq. (19) leads to the following flutter eigenvalue problem

$$\left[\lambda^2\mathbf{M}_{\mathsf{AE}}(\lambda) + \lambda\mathbf{C}_{\mathsf{AE}}(\lambda) + \mathbf{K}_{\mathsf{AE}}(\lambda)\right]\widetilde{\mathbf{X}} = \mathbf{0}, \tag{20}$$

where the aeroelastic matrices $\mathbf{M}_{\mathsf{AE}}(\lambda)$, $\mathbf{C}_{\mathsf{AE}}(\lambda)$ and $\mathbf{K}_{\mathsf{AE}}(\lambda)$ are defined as

$$\begin{aligned} \mathbf{M}_{\mathsf{AE}}(\lambda) &\equiv \mathbf{M}_\mathsf{S} - \mathbf{F}_{\dot{\Gamma}}[\widetilde{\mathbf{A}}(\lambda)]^{-1}\mathbf{b}_{\mathsf{S}\dot{\mathsf{X}}}, \\ \mathbf{C}_{\mathsf{AE}}(\lambda) &\equiv -\mathbf{F}_{\dot{\Gamma}}[\widetilde{\mathbf{A}}(\lambda)]^{-1}\mathbf{b}_\mathsf{X} - \mathbf{F}_\Gamma[\widetilde{\mathbf{A}}(\lambda)]^{-1}\mathbf{b}_{\mathsf{S}\dot{\mathsf{X}}}, \\ \mathbf{K}_{\mathsf{AE}}(\lambda) &\equiv \mathbf{K}_\mathsf{S} - \mathbf{F}_\Gamma[\widetilde{\mathbf{A}}(\lambda)]^{-1}\mathbf{b}_\mathsf{X}. \end{aligned} \tag{21}$$

It is worth noting that since the aeroelastic matrices in Eq. (21) depend on λ, the eigenvalues and eigenvectors of Eq. (20) must be searched using an iterative procedure. Moreover, assuming that the aerodynamic terms in the model depend only on λ, with no further assumptions in terms of harmonic behavior, the proposed solution methodology falls within the class of the p-methods.

3. Numerical results

In this section, the proposed aeroelastic formulation is tested and validated against numerical and experimental results either obtained via existing commercial software libraries or available in the literature. The methodology is implemented within the in-house python framework for scientific computing `PySCo`,[1] whereas the employed commercial library is `NASTRAN`, which implements the standard finite element method coupled with the doublet lattice method.

[1] https://gitlab.com/aeropa/pysco

Different DG_p schemes are tested for both beam theories (BT_n) and plate theories (PT_n), where the subscript n denote the order of the kinematics polynomial expansion over the transverse section of the beam or along the thickness of the plate while the subscript p denote the displacement expansion order over the beam span or the plate plane.

The performed tests are presented first for the analysis of a single lamina and then for various multilayered composite wings considering different stacking sequences and sweep angles. In all cases, the wing has half span $b/2 = 305\,\mathrm{mm}$, chord $c = 76.2\,\mathrm{mm}$ and thickness $\zeta = 0.804\,\mathrm{mm}$. Each layer of the laminated plate is an orthotropic material with $E_{11} = 98.0\,\mathrm{GPa}$, $E_{22} = E_{33} = 7.9\,\mathrm{GPa}$, $G_{23} = G_{13} = G_{12} = 5.6\,\mathrm{GPa}$, $\nu_{23} = \nu_{13} = \nu_{12} = 0.28\,\mathrm{GPa}$ and $\rho = 1520\,\mathrm{kg/m^3}$. The geometry and the material properties are taken from [51]. The results are presented in terms of eigenvalues λ and eigenvectors $\widetilde{\mathbf{X}}$ obtained as solutions of Eq. (20). The eigenvalues are reported in terms of non-dimensional real part $\widetilde{\omega}$ and imaginary part $\widetilde{\sigma}$ defined as

$$\widetilde{\omega} \equiv \frac{\omega}{\omega_{\mathrm{ref}}}, \quad \text{and} \quad \widetilde{\sigma} \equiv \frac{\sigma}{\omega_{\mathrm{ref}}}, \quad \text{with} \quad \omega_{\mathrm{ref}} \equiv \frac{\zeta}{b^2}\sqrt{\frac{E_{11}}{\rho}}. \tag{22}$$

Eventually, air is assumed to have density $\rho_\infty = 1.226\,\mathrm{kg/m^3}$.

3.1. Single lamina rectangular wing

The first set of tests investigates the accuracy and convergence of the proposed formulation for an unswept rectangular wing made of a single lamina, with lamination angle $\theta = 0$, subject to a free stream-velocity $V_\infty = 20\,\mathrm{m/s}$ and angle of attack $\alpha = 0°$. The plots reported in Figs. 2 and 3 show the values of $\widetilde{\omega}_k$ and $\widetilde{\sigma}_k$, respectively, with $k = 1, \ldots, 4$, for the first four eigenvalues as functions of the number of structural degrees of freedom (DOF). In the figures, from top to bottom, the computed eigenvalues are ordered in the four rows by increasing magnitude while each column is associated with a different structural theory. Each curve is obtained by changing the number of mesh elements and corresponds to a different DG_p scheme. The plots also show the results computed with the FEM plate model available in NASTRAN, and a dark grey area and a light grey area, which denote the regions of less than 1% and 5% deviation, respectively, from the values obtained with the finest FEM mesh. Both the present solution and the NASTRAN solution are computed using an aerodynamic mesh consisting of 16×64 bound vortexes.

The comparison between the results obtained by the proposed formulation and those obtained with NASTRAN confirms the accuracy of the DG-UVLM framework and shows the computational savings in terms of degrees of freedom that may be achieved via high-order displacement expansions, especially when higher order modes are of interest. The largest difference, which is less than 7.6%, is observed for the real part of the fourth eigenvalue and is attributed to the different aerodynamic model adopted in the present work and in NASTRAN.

A complete flutter analysis is eventually performed by studying the effect of the free-stream velocity V_∞. Fig. 4 shows the real part and the imaginary part of the first four eigenvalues plotted as functions of the free-stream velocity and computed with the proposed formulation using the DG_5 (PT_1) scheme and with NASTRAN. A satisfying match between the proposed and reference solution is attained and the flutter condition, identified when the real part of an eigenvalue first becomes positive, is correctly predicted.

3.2. Multilayered wing

After validating the DG-UVLM framework for flutter analysis of the single lamina, a set of flutter analyses for laminated composite wings is performed to ensure that the proposed formulation correctly predicts aeroelastic quantities of interest, such as the flutter velocity and the flutter frequency, for different stacking sequences and sweep angles.

(Figs. 5a), (5b) and (5c) show the real and imaginary parts of the aeroelastic eigenvalues as functions of the free-stream velocity for multilayered wing plates with stacking sequences $[90_2, 0]_\mathrm{S}$, $[45_2, 90]_\mathrm{S}$, and $[\pm 45, 90]_\mathrm{S}$ respectively. The results are computed using a DG_5 (PT_1) scheme and compared with those provided by FEM. As in the case of the single lamina, a satisfying match between the proposed and the reference solution is obtained, with the largest discrepancies observed for the real part of the first mode after a certain speed and likely due to the different aerodynamic model. A similar analysis is performed for the multilayered plate wing with stacking sequence $[60_2, 90]_\mathrm{S}$ that has been analyzed in Ref. [52] with a high-order FEM coupled with the Theodorsen theory. The results obtained by the present method, NASTRAN, and the method proposed in the literature are reported in Fig. 6. All methods show a satisfactory agreement up to the flutter speed, beyond which the method developed in Ref. [52] exhibits some differences compared to the other two, which may be attributed to the different aerodynamic model adopted. The computed values of flutter speeds and frequencies for the considered laminated wings are reported in Table 1 and are compared with numerical and experimental results available in the literature, further confirming the accuracy of the proposed formulation.

Eventually, the eigenmodes associated with the four eigenvalues computed near the onset of the flutter phenomenon, i.e., for $V_\infty = 23\,\mathrm{m/s}$, for the multilayered plate wing with stacking sequence $[90_2, 0]_\mathrm{S}$ are displayed in Fig. 7. In the figure, the colored contour plots show the u_3 displacement component computed employing the DG_5 (PT_1) scheme while the black continuous lines represent the contour levels of the same field obtained with the FEM solution. A fully satisfying match between the two solutions is observed.

As a final test, a backward swept laminated wing with $\Lambda = 30°$ is considered. The stacking sequence of the considered laminate is $[67.5, -22.5, -67.5, 22.5]_\mathrm{S}$ with a thickness sequence of $[0.09, 0.12, 0.16, 0.63]_\mathrm{S}$, where each term indicates the thickness ratio of each ply with respect to the half of the thickness of the laminate. Table 2 shows the comparison of the computed velocities and frequencies at the onset of the flutter instability. Present results are computed with a polynomial expansion of the fifth order along the y axis, i.e., the DG_5 scheme, using one structural element with three different high-order beam structural theory, namely BT_2, BT_3 and BT_4. As a benchmark, present result are compared against those found in Ref. [36], which are obtained using a FEM-DLM approach adopting the same structural theory and 15 structural element along the span of the swept wing. For each model the number of DOF is reported, showing that the proposed formulation allows achieving convergence with fewer degrees of freedom.

4. Discussion

In this section, some remarks about the potential, limitations and future developments of the proposed formulation are discussed.

First, considering that multilayered plate wings with rectangular cross sections have been analyzed in the present tests, further investigations could explore the ability of the proposed variable-order discontinuous Galerkin method to resolve wings with more complex geometries, featuring for example general cross section, including airfoils, or winglets, and/or internal structure, including ribs, stiffeners and cut-outs. In addition, more advanced materials, such as variable angle tow composite laminates, could be incorporated to increase the aeroelastic-tailoring capability of the proposed tool [11,54].

On the other hand, the proposed model is currently limited to small strains structural theories and potential aerodynamics. However, especially in modern high aspect-ratio wings/aircraft, large displacements and strains and/or non-linear aerodynamics play a remarkable role in complex phenomena such as limit cycle oscillations and stall flutter, as discussed in several works in the literature. [55–60]. The proposed method could therefore be extended by including finite-strain structural

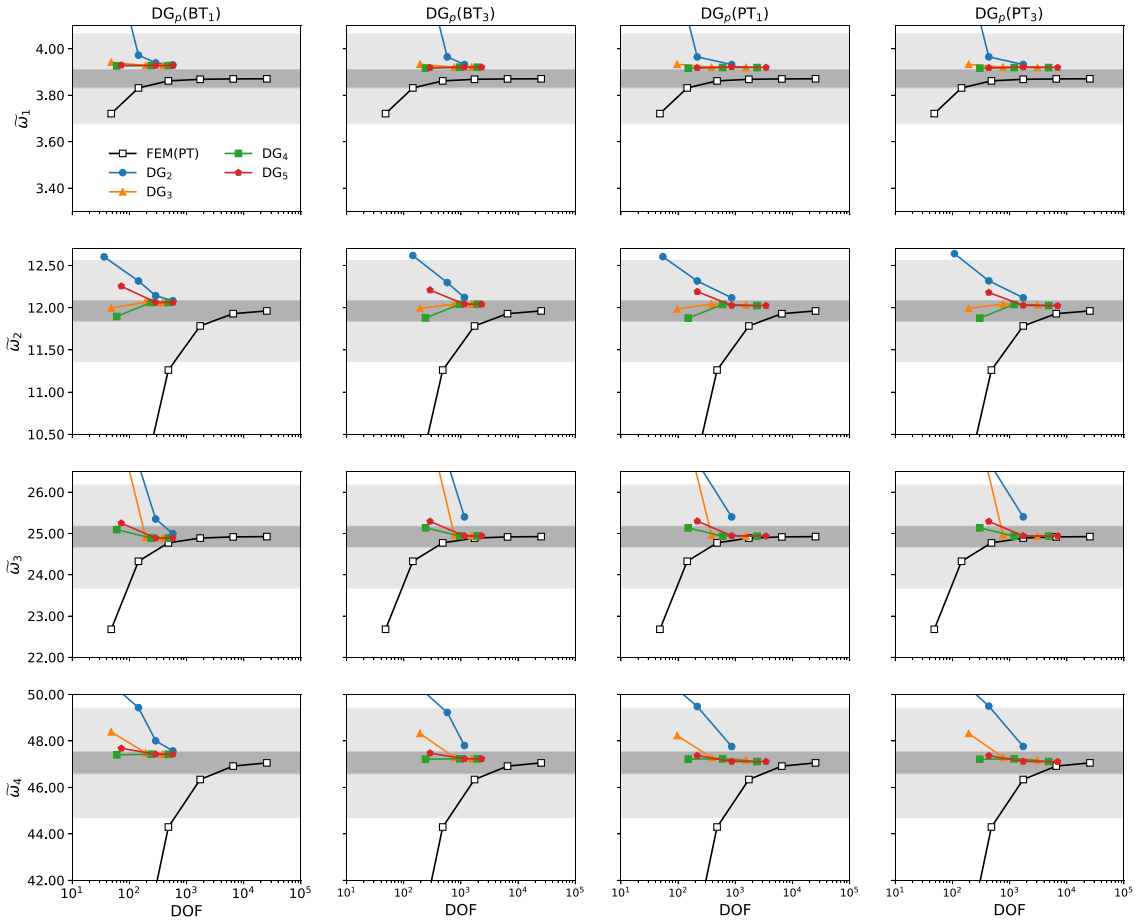

Fig. 2. Convergence analysis of the imaginary part $\widetilde{\omega}_k$ of the aeroelastic eigenvalues as a function of the structural DOF for different DG$_p$ schemes, represented by colored markers, for a single-lamina rectangular wing subject to a free stream velocity $V_\infty = 20\,\mathrm{m/s}$. From left to right, the four columns report values computed using the BT$_1$, BT$_3$, PT$_1$, and PT$_3$ theories, respectively. The obtained results are compared with those obtained with NASTRAN and represented by white markers connected by black lines. The darker and lighter gray areas denote the region of less than 1% and 5% deviation from the reference converged values.

Table 1
Flutter speeds and frequencies for composite laminated wings with stacking sequences $[90_2, 0]_S$, $[45_2, 90]_S$, $[\pm 45, 90]_S$ and $[60_2, 90]_S$ computed with the propose approach adopting a DG$_5$(PT$_1$) scheme and compared with both numerical and experimental results available in the literature.

Laminate	V_f [m/s]				ω_f [Hz]		
	DG$_5$ PT$_1$	Ref. [52][a]	Ref. [53][a]	Ref. [51][b]	DG$_5$ PT$_1$	Ref. [52][a]	Ref. [51][b]
$[90_2, 0]_S$	23.34	23.2	23.0	25	26.48	27.33	25
$[45_2, 90]_S$	26.49	29.6	27.5	28	22.84	25.04	28
$[\pm 45, 90]_S$	40.92	47.3	40.1	>32	48.17	31.48	39
$[60_2, 90]_S$	25.80	27.6	27.1	27	26.40	27.22	31

[a] Numerical.
[b] Experimental.

Table 2
Flutter velocities and frequencies for composite laminated swept wing with stacking sequence $[67.5, -22.5, -67.5, 22.5]_S$, computed with the proposed approach adopting three high-order beam theories and compared with numerical results of Ref. [36].

Model	Present			Ref.[36]		
	V_f [m/s]	ω_f [Hz]	DOF	V_f [m/s]	ω_f [Hz]	DOF
BT$_2$	31.920	26.137	162	38.703	28.394	828
BT$_3$	31.813	26.127	288	31.957	26.479	1380
BT$_4$	31.751	26.061	450	31.688	26.523	2070

theories and/or more complex aerodynamics [24,25], thus enabling the analysis of such phenomena. Incorporating large displacements and the ability to capture the interaction of multiple lifting surfaces may enable the flight dynamic analysis of flexible aircraft [34].

From the numerical point of view, the present work has compared the convergence and performance of the proposed DG-UVLM with standard FE-DLM methods widely employed in industrial applications, demonstrating the relative competitiveness. However, other efficient methods for aeroelastic analysis have been proposed in the literature [60], including for example the Differential Quadrature Method (DQM), which has been shown to offer computational benefits in terms of degrees of freedom and processing time with respect to standard FEs; Refs. [61,62] propose the use of DQM for subsonic and supersonic flutter analysis, also mentioning the achieved computational benefits. To the best of the authors' knowledge however, no systematic investigation has been performed on the relative performance of DQM and other techniques, including DG-UVLM, which could form the objective of further studies.

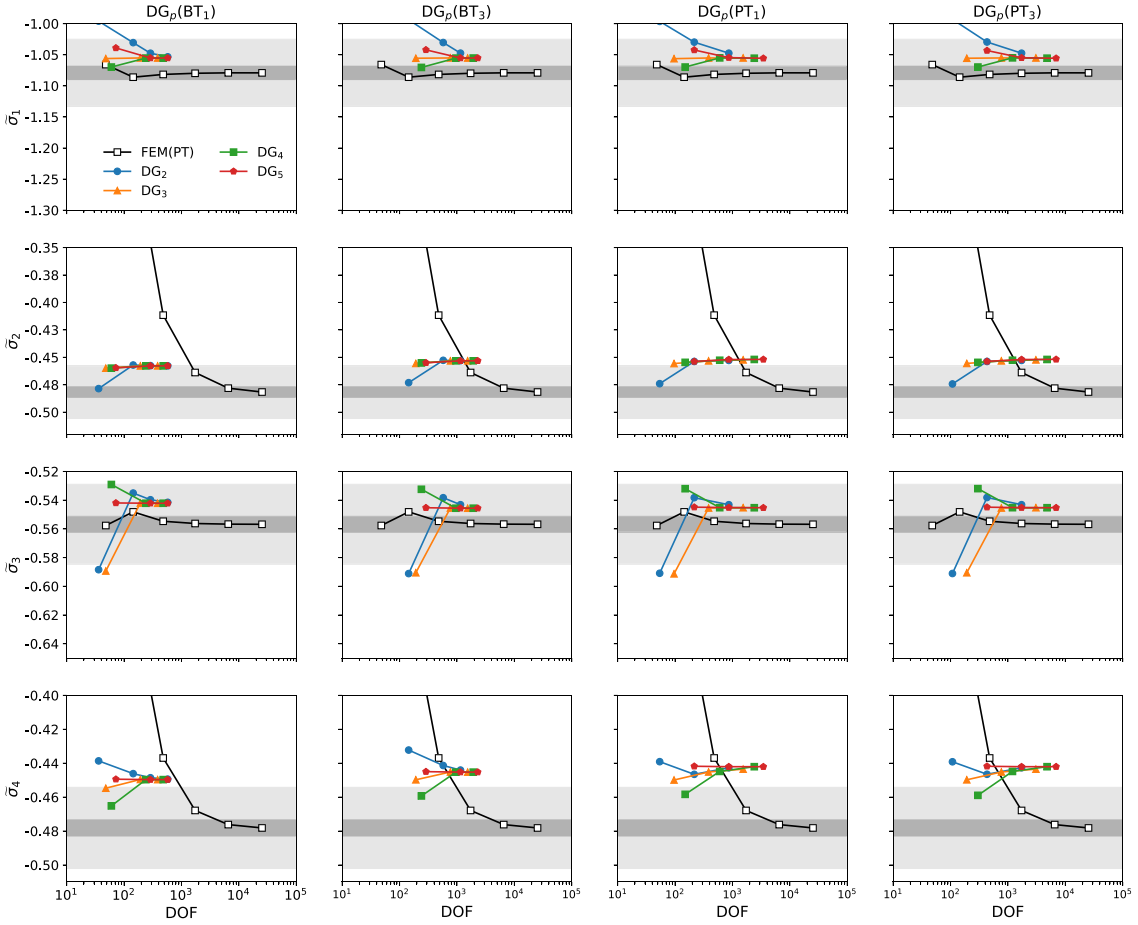

Fig. 3. Convergence analysis of the real part $\widetilde{\sigma}_k$ of the aeroelastic eigenvalues as a function of the structural DOF for different DG$_p$ schemes, represented by colored markers, for a single-lamina rectangular wing subject to a free stream velocity $V_\infty = 20\,\mathrm{m/s}$. From left to right, the four columns report values computed using the BT$_1$, BT$_3$, PT$_1$, and PT$_3$ theories, respectively. The obtained results are compared with those obtained with NASTRAN and represented by white markers connected by black lines. The darker and lighter gray areas denote the region of less than 1% and 5% deviation from the reference converged values.

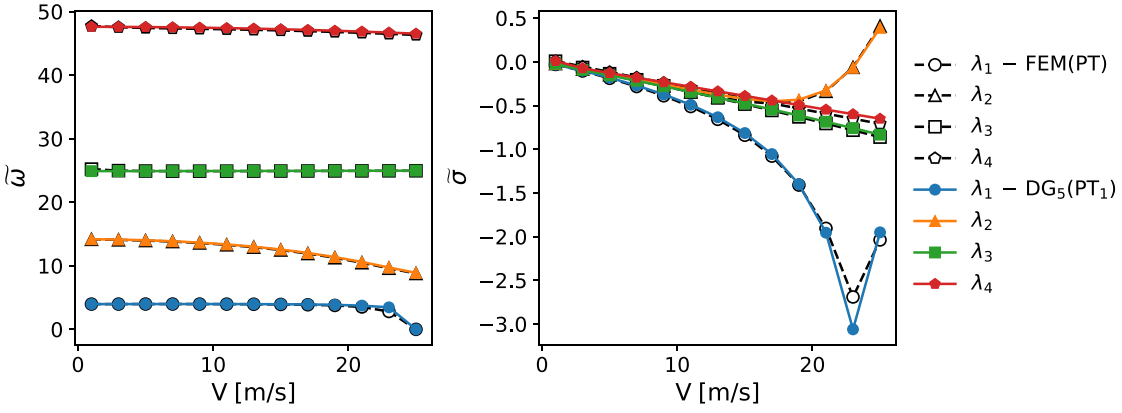

Fig. 4. Real and imaginary parts of aeroelastic eigenvalues as a function of the free-stream velocity V_∞ of the first four modes of a single-lamina cantilever wing plate. Colored markers correspond to values computed using the present DG$_5$ (PT$_1$) scheme, while white markers connected by dashed black lines correspond to eigenvalues computed using NASTRAN.

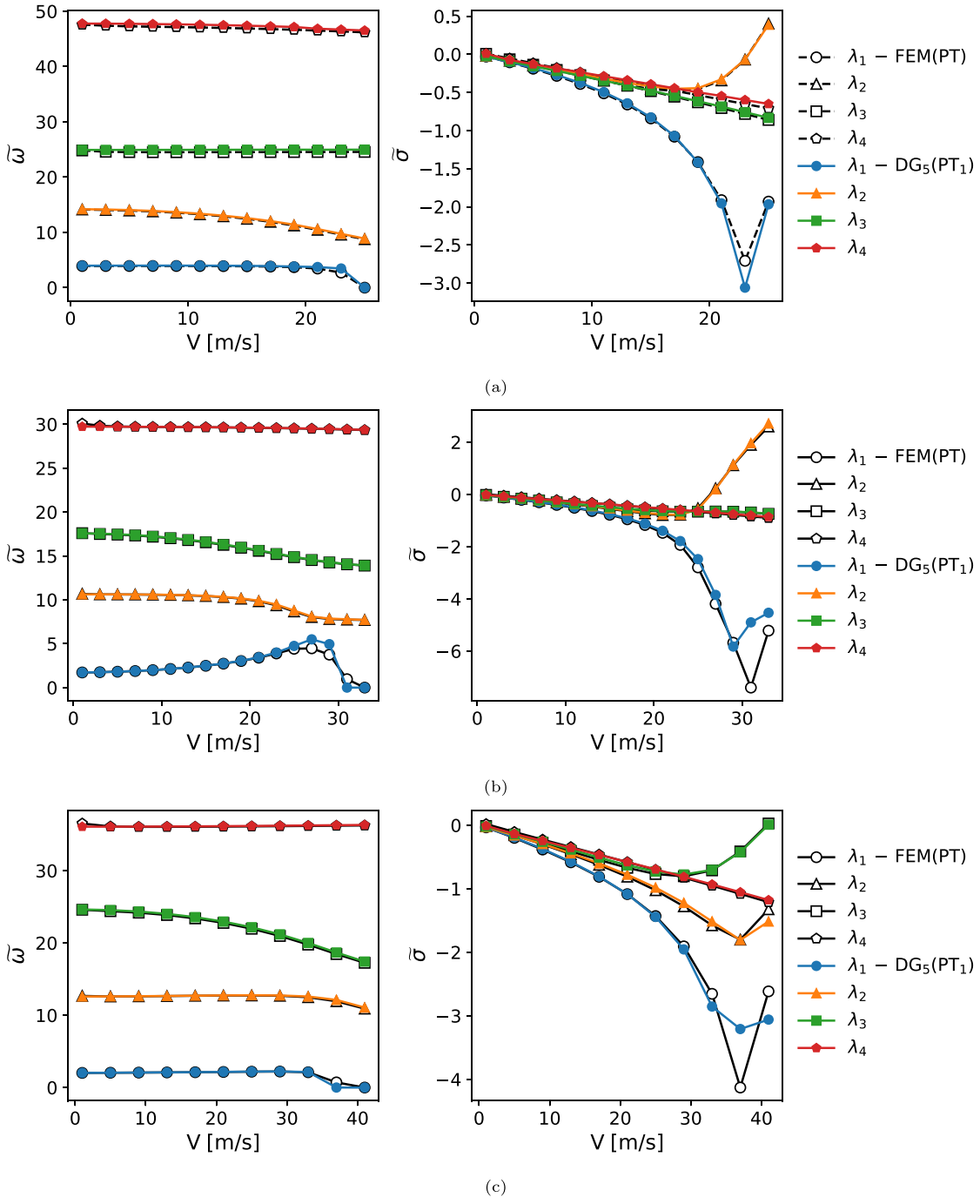

Fig. 5. Real and imaginary parts of aeroelastic eigenvalues as functions of the free-stream speed V_∞ for three multilayered wing plates with stacking sequences: (a) $[90_2, 0]_S$, (b) $[45_2, 90]_S$, and (c) $[\pm 45, 90]_S$. Colored markers correspond to values computed using the present DG$_5$ (PT$_1$) scheme, while white markers connected by dashed black lines correspond to eigenvalues computed using NASTRAN.

Eventually, considering the capability of higher-order models to capture structural damage and its effects [63,64], the framework could be enhanced to investigate how such damage affects critical aerodynamic stability thresholds [65].

Conclusions

In this study, a novel computational tool for the aeroelastic flutter analysis of laminated composite wings has been developed, implemented, tested and validated. The framework couples a discontinuous Galerkin formulation, based on a variable order kinematic model, for

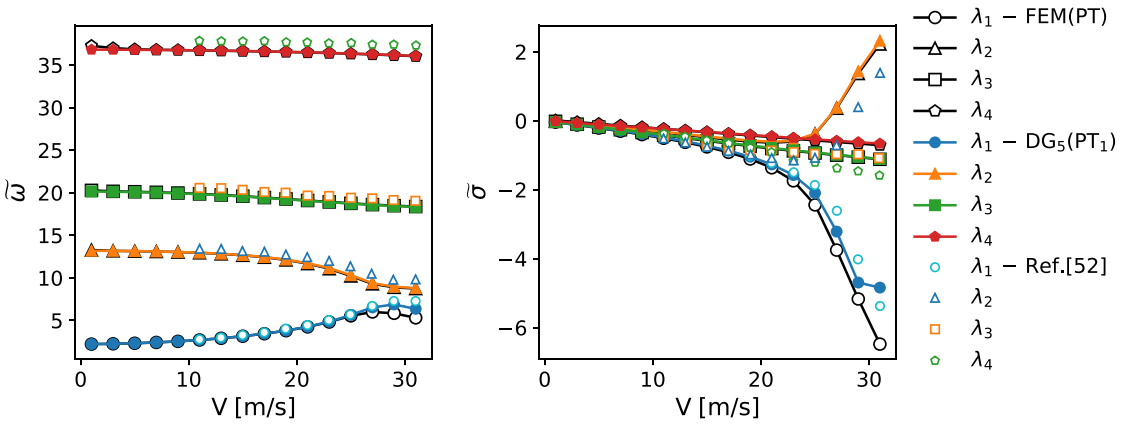

Fig. 6. Real and imaginary parts of aeroelastic eigenvalues as a function of the free-stream speed V_∞ of the first four modes of a laminated cantilever wing plate with stacking sequence $[60_2, 90]_S$ obtained by a DG_5 (PT_1) scheme. Present results are compared with those provided by the NASTRAN SOL 145 and those found in Ref. [52].

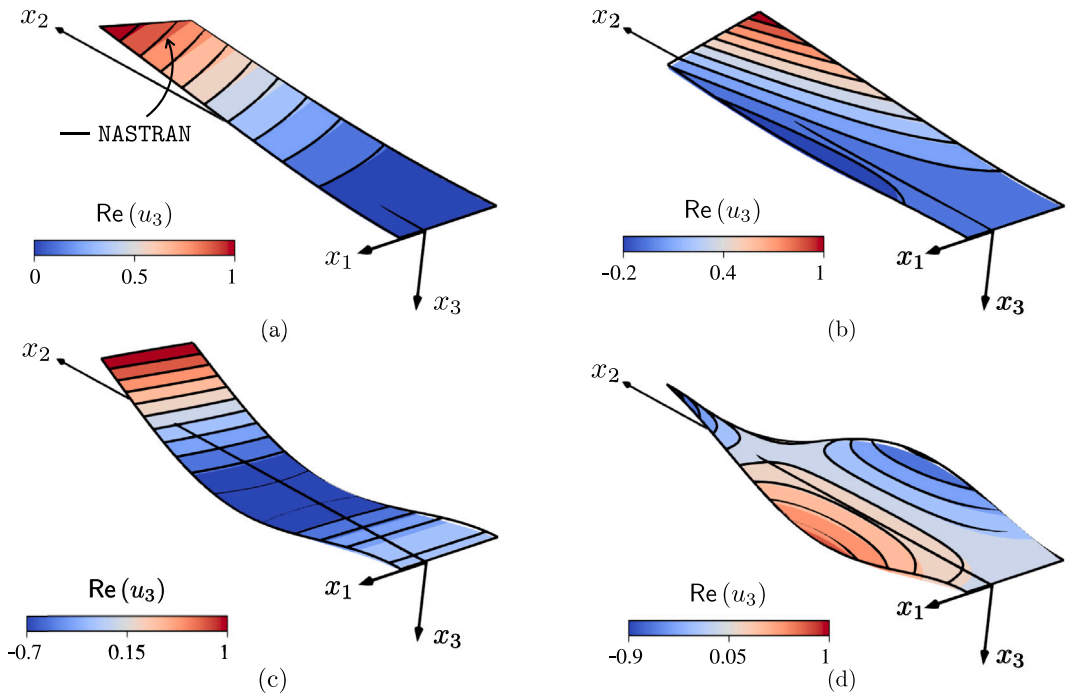

Fig. 7. Modal shapes of the first four aeroelastic modes of the $[90_2, 0]_S$ laminated composite wing plate at $V_\infty = 23$ m/s. Colored contour plots correspond to the u_3 displacement component obtained by the $DG_5(PT_1)$ scheme, while the black continuous lines correspond to the contour levels of the FEM solution.

structural analysis with an unsteady vortex lattice method for solving the aerodynamic problem. This integrated approach provides a flexible and efficient tool capable of accurately representing the aeroelastic response of composite structures with variable order approximations, including beam and plate theories. Validation against literature data and standard commercial aeroelastic software has demonstrated the accuracy, robustness and efficiency as well as the computational savings offered by the proposed methodology.

CRediT authorship contribution statement

Dario Campagna: Writing – review & editing, Writing – original draft, Visualization, Validation, Software, Methodology, Investigation, Data curation. **Ivano Benedetti:** Writing – review & editing, Writing – original draft, Supervision, Methodology, Formal analysis, Conceptualization. **Vincenzo Gulizzi:** Writing – review & editing, Writing – original draft, Validation, Supervision, Software, Project administration, Methodology, Funding acquisition, Formal analysis, Conceptualization.

Declaration of competing interest

Authors' declare that they have no known competing financial interests or personal relationships that could have appeared to influence the work reported in this paper.

Acknowledgments

DC and VG acknowledge the support by the European Union – Next Generation EU - PNRR M4 - C2 - investimento 1.1: Fondo per il Programma Nazionale di Ricerca e Progetti di Rilevante Interesse Nazionale (PRIN) - PRIN 2022 cod.2022AALLEC dal titolo "Hydrodynamic devices for micro-particle trapping and vibrational energy harvesting (HYDRA), Italy" CUP B53D23005770006. VG also acknowledges the support of the Department of Engineering of the University of Palermo, Italy, Italy through the grant *Gruppi di ricerca 2022*.

Data availability

Data will be made available on request.

References

[1] Wu T, Kareem A, Ge Y. Linear and nonlinear aeroelastic analysis frameworks for cable-supported bridges. Nonlinear Dynam 2013;74:487–516. http://dx.doi.org/10.1007/s11071-013-0984-7.

[2] Dongmei H, Ledong Z, Quanshun D, Xue Z, Wei C. Aeroelastic and aerodynamic interference effects on a high-rise building. J Fluids Struct 2017;69:355–81. http://dx.doi.org/10.1016/j.jfluidstructs.2017.01.007.

[3] Marshall J, Imregun M. A review of aeroelasticity methods with emphasis on turbomachinery applications. J Fluids Struct 1996;10(3):237–67. http://dx.doi.org/10.1006/jfls.1996.0015, https://www.sciencedirect.com/science/article/pii/S0889974696900158.

[4] Hou T, Wei X, Iqbal AA, Yang X, Wang J, Ren Y, et al. Advances in biomedical fluid–structure interaction: Methodologies and applications from an interfacing perspective. Phys Fluids 2024;36(2):021301. http://dx.doi.org/10.1063/5.0189218, arXiv:https://pubs.aip.org/aip/pof/article-pdf/doi/10.1063/5.0189218/19581812/021301_1_5.0189218.pdf.

[5] Zhang P, Huang S. Review of aeroelasticity for wind turbine: Current status, research focus and future perspectives. Front Energy 2011;5:419–34. http://dx.doi.org/10.1007/s11708-011-0166-6.

[6] Wang L, Liu X, Kolios A. State of the art in the aeroelasticity of wind turbine blades: Aeroelastic modelling. Renew Sustain Energy Rev 2016;64:195–210. http://dx.doi.org/10.1016/j.rser.2016.06.007, https://www.sciencedirect.com/science/article/pii/S1364032116302234.

[7] Ajaj RM, Parancheerivilakkathil MS, Amoozgar M, Friswell MI, Cantwell WJ. Recent developments in the aeroelasticity of morphing aircraft. Prog Aerosp Sci 2021;120:100682. http://dx.doi.org/10.1016/j.paerosci.2020.100682.

[8] Larsen A. Aerodynamics of the tacoma narrows bridge - 60 years later. Struct Eng Int 2000;10(4):243–8. http://dx.doi.org/10.2749/101686600780481356, arXiv:https://doi.org/10.2749/101686600780481356.

[9] Arioli G, Gazzola F. Torsional instability in suspension bridges: The tacoma narrows bridge case. Commun Nonlinear Sci Numer Simul 2017;42:342–57. http://dx.doi.org/10.1016/j.cnsns.2016.05.028, https://www.sciencedirect.com/science/article/pii/S1007570416301812.

[10] Hansen MH. Aeroelastic instability problems for wind turbines. Wind Energy 2007;10(6):551–77. http://dx.doi.org/10.1002/we.242, arXiv:https://onlinelibrary.wiley.com/doi/pdf/10.1002/we.242, https://onlinelibrary.wiley.com/doi/abs/10.1002/we.242.

[11] Stodieck O, Cooper JE, Weaver PM, Kealy P. Improved aeroelastic tailoring using tow-steered composites. Compos Struct 2013;106:703–15. http://dx.doi.org/10.1016/j.compstruct.2013.07.023, https://www.sciencedirect.com/science/article/pii/S0263822313003462.

[12] Werter N, De Breuker R. A novel dynamic aeroelastic framework for aeroelastic tailoring and structural optimisation. Compos Struct 2016;158:369–86. http://dx.doi.org/10.1016/j.compstruct.2016.09.044, https://www.sciencedirect.com/science/article/pii/S0263822316318669.

[13] Scott S, Capuzzi M, Langston D, Bossanyi E, McCann G, Weaver PM, et al. Effects of aeroelastic tailoring on performance characteristics of wind turbine systems. Renew Energy 2017;114:887–903. http://dx.doi.org/10.1016/j.renene.2017.06.048, https://www.sciencedirect.com/science/article/pii/S0960148117305530.

[14] Bai Y, Sun D, Lin J. Three dimensional numerical simulations of long-span bridge aerodynamics, using block-iterative coupling and des. Comput & Fluids 2010;39(9):1549–61. http://dx.doi.org/10.1016/j.compfluid.2010.05.005, https://www.sciencedirect.com/science/article/pii/S0045793010001118.

[15] Ilie M. A fully-coupled cfd/csd computational approach for aeroelastic studies of helicopter blade-vortex interaction. Appl Math Comput 2019;347:122–42. http://dx.doi.org/10.1016/j.amc.2018.10.069, https://www.sciencedirect.com/science/article/pii/S0096300318309433.

[16] Doi H, Alonso JJ. Fluid/structure coupled aeroelastic computations for transonic flows in turbomachinery. In: Volume 4: Turbo expo 2002, parts A and B. 2002, p. 787–94.

[17] Carstens V, Kemme R, Schmitt S. Coupled simulation of flow-structure interaction in turbomachinery. Aerosp Sci Technol 2003;7(4):298–306. http://dx.doi.org/10.1016/S1270-9638(03)00016-6, https://www.sciencedirect.com/science/article/pii/S1270963803000166.

[18] Phan HM, He L. Investigation of structurally and aerodynamically mistuned oscillating cascade using fully coupled method. J Eng Gas Turbines Power 2021;144(3):031009. http://dx.doi.org/10.1115/1.4052751, arXiv:https://asmedigitalcollection.asme.org/gasturbinespower/article-pdf/144/3/031009/6807928/gtp_144_03_031009.pdf.

[19] Mao W, Caballero A, McKay R, Primiano C, Sun W. Fully-coupled fluid–structure interaction simulation of the aortic and mitral valves in a realistic 3D left ventricle model. PLoS One 2017;12(9):1–21. http://dx.doi.org/10.1371/journal.pone.0184729.

[20] Farhat C, Geuzaine P, Brown G. Application of a three-field nonlinear fluid–structure formulation to the prediction of the aeroelastic parameters of an F-16 fighter. Comput & Fluids 2003;32(1):3–29. http://dx.doi.org/10.1016/S0045-7930(01)00104-9, https://www.sciencedirect.com/science/article/pii/S0045793001001049.

[21] Mian HH, Wang G, Ye Z-Y. Numerical investigation of structural geometric nonlinearity effect in high-aspect-ratio wing using CFD/CSD coupled approach. J Fluids Struct 2014;49:186–201. http://dx.doi.org/10.1016/j.jfluidstructs.2014.04.011, https://www.sciencedirect.com/science/article/pii/S0889974614000875.

[22] Huang C, Huang J, Song X, Zheng G, Yang G. Three dimensional aeroelastic analyses considering free-play nonlinearity using computational fluid dynamics/computational structural dynamics coupling. J Sound Vib 2021;494:115896. http://dx.doi.org/10.1016/j.jsv.2020.115896, https://www.sciencedirect.com/science/article/pii/S0022460X20307355.

[23] Xu M, An X, Kang W, Li G. Modern computational aeroelasticity. Berlin, Boston: De Gruyter; 2021, http://dx.doi.org/10.1515/9783110576689, [cited 2024-03-06].

[24] Grifò M, Da Ronch A, Benedetti I. A computational aeroelastic framework based on high-order structural models and high-fidelity aerodynamics. Aerosp Sci Technol 2023;132:108069. http://dx.doi.org/10.1016/j.ast.2022.108069, https://www.sciencedirect.com/science/article/pii/S127096382200743X.

[25] Grifò M, Gulizzi V, Milazzo A, Da Ronch A, Benedetti I. High-fidelity aeroelastic transonic analysis using higher-order structural models. Compos Struct 2023;321:117315. http://dx.doi.org/10.1016/j.compstruct.2023.117315, https://www.sciencedirect.com/science/article/pii/S026382232300661X.

[26] Yu DO, Kwon OJ. Predicting wind turbine blade loads and aeroelastic response using a coupled CFD-CSD method. Renew Energy 2014;70:184–96. http://dx.doi.org/10.1016/j.renene.2014.03.033, special issue on aerodynamics of offshore wind energy systems and wakes, https://www.sciencedirect.com/science/article/pii/S0960148114001803.

[27] Sayed M, Lutz T, Krämer E, Shayegan S, Wüchner R. Aeroelastic analysis of 10 mw wind turbine using cfd–csd explicit fsi-coupling approach. J Fluids Struct 2019;87:354–77.

[28] Sayed M, Bucher P, Guma G, Lutz T, Wüchner R. Aeroelastic simulations based on high-fidelity cfd and csd models. In: Handbook of wind energy aerodynamics. 2022, p. 1–76. http://dx.doi.org/10.1007/978-3-030-05455-7_22-1.

[29] Smith M, Patil M, Hodges D. Cfd-based analysis of nonlinear aeroelastic behavior of high-aspect ratio wings. In: 19th AIAA applied aerodynamics conference. 2001, p. 1582.

[30] Garcia JA. Numerical investigation of nonlinear aeroelastic effects on flexible high-aspect-ratio wings. J Aircr 2005;42(4):1025–36.

[31] Jung YS, Yu DO, Kwon OJ. Aeroelastic analysis of high-aspect-ratio wings using a coupled cfd-csd method. Trans Japan Soc Aeronaut Space Sci 2016;59(3):123–33.

[32] Katz J, Plotkin A. Low-speed aerodynamics. Cambridge aerospace series, 2nd ed.. Cambridge University Press; 2001, http://dx.doi.org/10.1017/CBO9780511810329.

[33] van Zyl LH, Mathews EH. Aeroelastic analysis of t-tails using an enhanced doublet lattice method. J Aircr 2011;48(3):823–31. http://dx.doi.org/10.2514/1.C001000, arXiv:https://doi.org/10.2514/1.C001000.

[34] Murua J, Palacios R, Graham JMR. Applications of the unsteady vortex-lattice method in aircraft aeroelasticity and flight dynamics. Prog Aerosp Sci 2012;55:46–72. http://dx.doi.org/10.1016/j.paerosci.2012.06.001, https://www.sciencedirect.com/science/article/pii/S0376042112000620.

[35] Carrera E, Varello A, Demasi L. A refined structural model for static aeroelastic response and divergence of metallic and composite wings. CEAS Aeronaut J 2013;4(2):175–89.

[36] Petrolo M. Flutter analysis of composite lifting surfaces by the 1d carrera unified formulation and the doublet lattice method. Compos Struct 2013;95:539–46. http://dx.doi.org/10.1016/j.compstruct.2012.06.021, https://www.sciencedirect.com/science/article/pii/S0263822312003108.

[37] Xie C, Wang L, Yang C, Liu Y. Static aeroelastic analysis of very flexible wings based on non-planar vortex lattice method. Chin J Aeronaut 2013;26(3):514–21. http://dx.doi.org/10.1016/j.cja.2013.04.048, https://www.sciencedirect.com/science/article/pii/S100093611300099X.

[38] Gulizzi V, Benedetti I. Computational aeroelastic analysis of wings based on the structural discontinuous Galerkin and aerodynamic vortex lattice methods. Aerosp Sci Technol 2024;144:108808. http://dx.doi.org/10.1016/j.ast.2023.108808, https://www.sciencedirect.com/science/article/pii/S1270963823007046.

[39] Campagna D, Gulizzi V, Benedetti I. A dg-vlm framework for computational static aeroelastic analysis of composite wings. Compos Struct 2025;353:118697.

[40] Vindigni CR, Mantegna G, Orlando C, Alaimo A, Berci M. A refined aeroelastic beam finite element for the stability analysis of flexible subsonic wings. Comput Struct 2025;307:107618.

[41] Gulizzi V, Benedetti I, Milazzo A. High-order accurate beam models based on discontinuous Galerkin methods. In: Aerotecnica missili & spazio. 2023, p. 1–16.

[42] Gulizzi V, Benedetti I, Milazzo A. An implicit mesh discontinuous Galerkin formulation for higher-order plate theories. Mech Adv Mater Struct 2020;27(17):1494–508.

[43] Gulizzi V, Benedetti I, Milazzo A. A high-resolution layer-wise discontinuous Galerkin formulation for multilayered composite plates. Compos Struct 2020;242:112137.
[44] Gulizzi V, Benedetti I, Milazzo A. High-order accurate transient and free-vibration analysis of plates and shells. J Sound Vib 2024;587:118479. http://dx.doi.org/10.1016/j.jsv.2024.118479, https://www.sciencedirect.com/science/article/pii/S0022460X24002426.
[45] Parenteau M, Laurendeau E. Nonlinear frequency-domain solver for vortex lattice method. AIAA J 2018;56(6):2242–51. http://dx.doi.org/10.2514/1.J056704.
[46] Gulizzi V, Benedetti I, Milazzo A. Discontinuous galerkin methods for solids and structures. In: Aliabadi MHF, Soboyejo WO, editors. Comprehensive Structural Integrity. 2nd ed.. Oxford: Elsevier; 2023, p. 348–77. http://dx.doi.org/10.1016/B978-0-12-822944-6.00024-4, https://www.sciencedirect.com/science/article/pii/B9780128229446000244.
[47] Reddy JN. Mechanics of laminated composite plates and shells: theory and analysis. CRC Press; 2003.
[48] Carrera E, Cinefra M, Petrolo M, Zappino E. Finite element analysis of structures through unified formulation. John Wiley & Sons; 2014.
[49] Demasi L, Ashenafi Y, Cavallaro R, Santarpia E. Generalized unified formulation shell element for functionally graded variable-stiffness composite laminates and aeroelastic applications. Compos Struct 2015;131:501–15. http://dx.doi.org/10.1016/j.compstruct.2015.05.022, https://www.sciencedirect.com/science/article/pii/S0263822315003876.
[50] Arnold DN, Brezzi F, Cockburn B, Marini LD. Unified analysis of discontinuous galerkin methods for elliptic problems. SIAM J Numer Anal 2002;39(5):1749–79.
[51] Hollowell SJ, Dugundji J. Aeroelastic flutter and divergence of stiffness coupled, graphite/epoxy cantilevered plates. J Aircr 1984;21(1):69–76.
[52] Bharati RB, Filippi M, Mahato PK, Carrera E. Flutter analysis of laminated composite structures using carrera unified formulation. Compos Struct 2020;253:112759.
[53] Kameyama M, Fukunaga H. Optimum design of composite plate wings for aeroelastic characteristics using lamination parameters. Comput Struct 2007;85(3–4):213–24.
[54] Wang Z, Wan Z, Groh RM, Wang X. Aeroelastic and local buckling optimisation of a variable-angle-tow composite wing-box structure. Compos Struct 2021;258:113201. http://dx.doi.org/10.1016/j.compstruct.2020.113201, https://www.sciencedirect.com/science/article/pii/S0263822320331275.
[55] Palacios R, Cesnik C. Static nonlinear aeroelasticity of flexible slender wings in compressible flow. In: 46th AIAA/aSME/ASCE/AHS/aSC structures, structural dynamics and materials conference. 2005, p. 1945. http://dx.doi.org/10.2514/6.2005-1945.
[56] Xiang J-W. Stall flutter analysis of high-aspect-ratio composite wing. Chin J Aeronaut 2006;19(1):36–43.
[57] Farsadi T, Asadi D, Kurtaran H. Nonlinear flutter response of a composite plate applying curvilinear fiber paths. Acta Mech 2020;231(2):715–31.
[58] Chao A, Chao Y, Changchuan X, Lan Y. Flutter and gust response analysis of a wing model including geometric nonlinearities based on a modified structural rom. Chin J Aeronaut 2020;33(1):48–63.
[59] Farsadi T, Rahmanian M, Kayran A. Reduced order nonlinear aeroelasticity of swept composite wings using compressible indicial unsteady aerodynamics. J Fluids Struct 2020;92:102812.
[60] Antimirova E, Jung J, Zhang Z, Machuca A, Gu GX. Overview of computational methods to predict flutter in aircraft. J Appl Mech 2024;91(5).
[61] Niu Y, Wang Z, Zhang W. Flutter analysis of a supersonic composite airfoil skin by using the differential quadrature method. Mech Compos Mater 2012;48:547–58.
[62] Ghalandari M, Shamshirband S, Mosavi A, w. Chau K. Flutter speed estimation using presented differential quadrature method formulation. Eng Appl Comput Fluid Mech 2019;13(1):804–10.
[63] Campagna D, Milazzo A, Benedetti I, Oliveri V. A non-linear ritz method for progressive failure analysis of variable angle tow composite laminates. Mech Adv Mater Struct 2023;30(5):995–1008.
[64] Campagna D, Oliveri V, Benedetti I. An adaptive ritz formulation for progressive damage modelling in variable angle tow composite plates. Compos Struct 2024;331:117915. http://dx.doi.org/10.1016/j.compstruct.2024.117915, https://www.sciencedirect.com/science/article/pii/S0263822324000436.
[65] Hoseini HS, Hodges DH. Aeroelastic stability analysis of damaged high-aspect-ratio composite wings. J Aircr 2019;56(5):1794–808. http://dx.doi.org/10.2514/1.C035098, arXiv:https://doi.org/10.2514/1.C035098.